International Journal of Multiphase Flow 140 (2021) 103650

Contents lists available at ScienceDirect

International Journal of Multiphase Flow

journal homepage: www.elsevier.com/locate/ijmulflow

The effect of Stefan flow on Nusselt number and drag coefficient of spherical particles in non-isothermal gas flow

Thamali R. Jayawickrama[a,*], Nils Erland L. Haugen[b,c], Matthaus U. Babler[d], M.A. Chishty[a], Kentaro Umeki[a]

[a] Energy Engineering, Div. Energy Science, Luleå University of Technology, Luleå 971 87, Sweden
[b] Department of Energy and Process Engineering, Norwegian University of Science and Technology, Kolbjørn Hejes vei 1 B, 7491 Trondheim, Norway
[c] Department of Thermal Energy, SINTEF Energy Research, Kolbjørn Hejes vei 1 A, 7491 Trondheim, Norway
[d] Department of Chemical Engineering, KTH Royal Institute of Technology, SE-10044 Stockholm, Sweden

ARTICLE INFO

Article history:
Received 17 August 2020
Revised 21 December 2020
Accepted 25 March 2021
Available online 29 March 2021

Keywords:
Drag coefficient
Nusselt number
Stefan flow
Boundary layer
multiphase reactive flow

ABSTRACT

A Stefan flow can be generated during a phase change or reactions of a particle immersed in a fluid. This study investigates the effect of Stefan flow on the exchange of momentum (drag coefficient (C_D)) and heat transfer (Nusselt number (Nu)) between the particle and bulk-fluid. Fully resolved simulations were carried out for a flow near a spherical particle immersed in a uniform bulk flow. The immersed boundary method is used for implementing fluid-solid interactions and the particle is considered as a static boundary with fixed boundary conditions. In a non-isothermal flow, the changes in thermophysical properties at the boundary layer played a role in the variation of C_D and Nu by a Stefan flow further. The previously developed model for the drag coefficient of a spherical particle in a uniform isothermal flow was modified for a uniform non-isothermal flow. The model is developed based on physical interpretation. A new model is developed for the Nusselt number for a spherical particle with a uniform Stefan flow combining available models in literature. The models are validated for Stefan Reynolds number $-8 \leqslant \mathrm{Re}_{sf,p} \leqslant 25$ and particle Reynolds number of $2 \leqslant \mathrm{Re}_f \leqslant 30$ in gas flow (i.e. Pr≈ 0.7).

1. Introduction

Particle-laden flows have many complexities due to *e.g.* flow separation, particle wakes, multi-particle effects, Stefan flow effects and reactions. Such flows are associated with physical effects that have a wide range of length and time scales. For example, the largest length scale in pulverized boilers (reactor) is $\mathcal{O}(10^1\mathrm{m})$ while the smallest physical scale (particle boundary layer) is $\mathcal{O}(10^{-5}\mathrm{m})$ and the smallest chemical scale is $\mathcal{O}(10^{-10}\mathrm{m})$. Therefore, it is currently impossible to resolve all scales in any numerical setup of practical relevance. This gap can be bridged by developing models describing the effects occurring at smaller scales (smallest physical/chemical scales). The smallest physical scales ($\mathcal{O}(10^{-5}\mathrm{m})$) can be studied through detailed numerical simulations. In contrast to experimental data, numerical simulations create a virtual environment that is much more versatile to elucidate the relevant transport phenomena and that can be used for developing models. In the current study, we investigate the Stefan flow effects in particle-laden flows using numerical simulations.

A Stefan flow is created when there is a net flow of gas/fluid towards or away from a solid surface that is reacting or undergoing a phase change (Murphy and Shaddix, 2003). Some examples are: evaporation, condensation and combustion of droplets as well as pulverized fuel combustion and gasification. The Stefan flow can affect the exchange of mass, momentum and heat between the surface and the bulk fluid in particle-laden flows. Models for Nusselt number (Nu), Sherwood number (Sh) and the drag coefficient (C_D) are used to calculate heat, mass and momentum transfer between the particle and the fluid, respectively. However, this study will only consider the Nusselt number and the drag coefficient.

In the past, the Stefan flow effect was considered for droplet evaporation and combustion (Renksizbulut and Yuen, 1983b; 1983a; Abramzon and Sirignano, 1989; Harpole, 1981). Lately, an interest for the effect of the Stefan flow has emerged for coal combustion applications due to high reactive gas concentration in Oxy-fuel combustion (O_2/CO_2) compared to air-fuel combustion (N_2/O_2). The importance of Stefan flow in Oxy-fuel combustion of coal is emphasized by Yu et al. (2013). According to them, a Ste-

* Corresponding author.
E-mail address: thamalirajika@gmail.com (T.R. Jayawickrama).

https://doi.org/10.1016/j.ijmultiphaseflow.2021.103650

Nomenclature

Roman Symbols

Symbol	Description (Units)
A	cross section area (m^2)
c_p	specific heat capacity (J kg^{-1} K^{-1})
D	diameter of the particle (m)
F	force (N)
h	heat transfer coefficient (W m^{-2} K^{-1})
$\overrightarrow{I}$	identity matrix (1)
L	latent heat of evaporation (J kg^{-1})
$\overrightarrow{n}$	unit normal vector (1)
p	pressure (Pa)
R	radius (m)
S	surface area (m^2)
T	temperature (K)
t	weighting factor (between 0 to 1) (-)
U	velocity (m s^{-1})
$\overrightarrow{u}$	velocity vector (m s^{-1})
V	volume (m^3)

Greek Symbols

δ	boundary layer thickness (m)
μ	viscosity (Pa s)
ρ	density (kg m^{-3})
τ	time scale (s)
λ	thermal conductivity (W m^{-1} K^{-1})

Subscripts

b	boiling point (-)
B	boundary layer (-)
∞	parameters calculated at the far-field condition (-)
f	parameters calculated at the film condition (when $t = 0.5$) (-)
l	liquid (-)
sf	with Stefan flow conditions (-)
p	parameters calculated at the particle surface (-)

Dimensionless numbers

B_T	Spalding heat transfer number ($B_T = \frac{c_p(T_b - T_\infty)}{L}$)
C_D	Drag coefficient ($C_D = \frac{F}{0.5\rho U^2 A}$)
Nu	Nusselt number ($\mathrm{Nu} = \frac{hd}{\lambda}$)
Pe	Peclet number ($\mathrm{Pe} = \mathrm{Re} \times \mathrm{Pr}$)
Pr	Prandtl number ($\mathrm{Pr} = \frac{c_p \mu}{\lambda}$)
Re	Reynolds number ($\mathrm{Re} = \frac{\rho U D}{\mu}$)

fan flow has a strong influence on the mass transfer rate in Zone II conversion (kinetically and diffusion controlled) while the effect is insignificant in Zone III (diffusion controlled) during burnout period. Still it is not clear from their results when Stefan flow can be neglected.

The main objective of the current paper is to study the effect of Stefan flow on Nusselt number and drag coefficient for non-isothermal conditions (*i.e.* when there is a temperature difference between particle and gas field). Even though the model is generic and meant to be applicable for a variety of conditions, it was developed and validated with a primary interest on entrained-flow biomass gasification. As summarized in the next section, we aim to fill a gap in knowledge and models, especially under the presence of large temperature differences (*i.e.* >100 K). Hereafter 'temperature difference (ΔT)' means the temperature difference between the solid particle (sphere) surface and the far-field of the fluid. Simulations resolving the boundary layer are carried out for a laminar flow surrounding a static spherical particle. Multi-component effects were avoided for the simplicity of work. The applicability of our model for the drag coefficient, developed in our previous work under isothermal conditions (Jayawickrama et al., 2019), is assessed and extended to non-isothermal conditions. In addition, a new model describing the effect of Stefan flow on the Nusselt number is developed.

2. Previous studies

2.1. Nusselt number at high temperature difference

The Nusselt number ($\mathrm{Nu}=hD/\lambda$) is usually expressed as a function of Reynolds number ($\mathrm{Re}=\rho UD/\mu$) and Prandtl number ($\mathrm{Pr}=c_p\mu/\lambda$). A Nusselt number formula that is applicable for both high and low temperature difference conditions is hard to find in the literature. Two popular models are the models of Whitaker (1972) and the model of Ranz-Marshall Ranz and Marshall (1952). The former reads as:

$$\mathrm{Nu} = 2 + (0.4\mathrm{Re}^{\frac{1}{2}} + 0.06\mathrm{Re}^{\frac{2}{3}})\mathrm{Pr}^{0.4}\left(\frac{\mu_\infty}{\mu_p}\right)^{\frac{1}{4}}, \quad (1)$$

where thermophysical properties (*i.e.* λ, ρ, μ, and c_p) for the calculation of Nusselt number, Reynolds number, and Prandtl number are based on far-field conditions, μ_∞ is the viscosity at far-field condition and μ_p is the viscosity at particle surface condition. The Ranz-Marshall model Ranz and Marshall (1952) is given as:

$$\mathrm{Nu} = 2 + 0.6\mathrm{Re}^{\frac{1}{2}}\mathrm{Pr}^{\frac{1}{3}}, \quad (2)$$

where thermophysical properties at film condition are used to calculate Nusselt number, Reynolds number and Prandtl numbers, instead of those at far-field conditions. Film condition is defined as the average between the far-field condition and the surface condition, i.e. $T_f = (T_\infty + T_p)/2$ where T_∞ and T_p are the far-field and surface temperatures, respectively. At low temperature differences and Reynolds numbers ($\approx 0 < \mathrm{Re} < 100$), the Whitaker model (Eq. 1) typically gives predictions that are closer to the actual values (Nikrityuk and Meyer, 2014), while the Ranz-Marshall model (Eq. (2)) can be applied for high temperature differences ($1 < \mathrm{Re} < 130$) (Ellendt et al., 2018).

There are numerous works on developing models for the Nusselt number associated with droplet evaporation. Evaporation at high temperature differences requires consideration of the variation of thermophysical properties, such as thermal conductivity (λ) and specific heat capacity (c_p). This effect can be accounted for through a correction factor for the Nusselt number (Harpole, 1981), or by introducing a reference temperature (Naraslmhan and Gauvin, 1967; Downingm, 1966; Yuen and Chen, 1978). The reference temperature is then calculated as follows:

$$T_t = tT_\infty + (1-t)T_p, \quad (3)$$

where t is weight factor.

2.2. Effect of Stefan flow on Nusselt number

Different models for the Nusselt number developed for evaporation of single droplets are summarized by Zhifu et al. (2013). They have categorized the available models into theoretical, numerical and experimental models. According to their comparisons, all the models are deviating from experimental results when the evaporation rates are high. Therefore, they have developed a model with a correction factor that is applicable for high evaporation rates as well. In this model, the Nusselt number is given as:

$$\mathrm{Nu}_{Zh} = f_T \mathrm{Nu}, \quad (4)$$

where

$$f_T = (1 + B_{Tp})^{-\frac{2}{3}}, \quad (5)$$

and

$$\mathrm{Nu} = 2 + 0.552\mathrm{Re}^{\frac{1}{2}}\mathrm{Pr}^{\frac{1}{3}}. \tag{6}$$

Here the Spalding heat transfer number (B_{Tp}) is defined as:

$$B_{Tp} = \frac{c_{p,p}(T_\infty - T_b)}{L}, \tag{7}$$

where L is latent heat of evaporation and T_b is the boiling point temperature. The Reynolds number is calculated based on properties at the particle surface, while the Prandtl number is calculated based on far-field condition. The Nusselt number is calculated based on properties at the particle surface condition. It is noticed that the model of Zhifu et al. (2013) has no explicit dependence on the Stefan flow. The effect of Stefan flow is accounted for indirectly through the evaporation rate, characterized by the Spalding heat transfer number.

Niazmand and Renksizbulut (2003) used the model developed for droplet evaporation by Renksizbulut & Yuen (Nu_{RY}) Renksizbulut and Yuen (1983a) for the generalized case of a Stefan flow:

$$\mathrm{Nu}_{RY} = \frac{2 + 0.57\mathrm{Re}^{1/2}\mathrm{Pr}^{1/3}}{(1 + B_{T_f})^{0.7}} \tag{8}$$

where the Reynolds number is calculated based on particle surface conditions, Prandtl number is calculated based on film condition and the Spalding heat transfer number is defined as:

$$B_{T_f} = \frac{\mathrm{PrRe}_{sf}}{\mathrm{Nu}}, \tag{9}$$

where

$$\mathrm{Re}_{sf} = \frac{\rho U_{sf} D}{\mu}, \tag{10}$$

is the Reynolds number based on the Stefan flow velocity (hereafter, called Stefan Reynolds number). The variation of thermophysical properties are neglected for Niazmand and Renksizbulut Niazmand and Renksizbulut (2003) and the selected range of Stefan flows was based on droplet evaporation ($0.01 \geqslant \frac{U_{sf}}{U_\infty} \geqslant 0.04$). Murphy & Shaddix Murphy and Shaddix (2003) have formulated a Nusselt number (Nu_M) correlation, for Stefan flow in a quiescent environment. Assuming constant properties, their expression reads as:

$$\mathrm{Nu}_M = \mathrm{Nu}\frac{(\mathrm{PrRe}_{sf})/\mathrm{Nu}}{e^{(\mathrm{PrRe}_{sf})/\mathrm{Nu}} - 1}, \tag{11}$$

where $\mathrm{Nu} = 2$ is the Nusselt number in a quiescent flow without Stefan flow. Recently, Kestel Kestel (2016) developed a new empirical model applicable for the convective flow environment based on his simulation data that gave better accuracy than the other available models. In this model, which is applicable for $\mathrm{Re} < 200$, $\mathrm{Re}_{sf} < 20$ and $0.744 < \mathrm{Pr} < 1.5$, the Nusselt number ($\mathrm{Nu}_K$) is given as:

$$\mathrm{Nu}_K = \mathrm{Nu}\exp\left(\frac{-0.54\,\mathrm{Pr}\,\mathrm{Re}_{sf}^{1.126}}{\mathrm{Nu}^{1.052}}\right), \tag{12}$$

where

$$\mathrm{Nu} = 2 + 0.39\mathrm{Re}^{0.56}\mathrm{Pr}^{0.45}. \tag{13}$$

In Eq. 12 and 13, all properties are calculated based on the reference temperature as defined in Eq. (3) when the weight factor is $t = 0.9$. This model has a large number of fitting parameters and it does agree better with simulation results. However, it does not necessarily represent the physical phenomena.

In summary, most of the currently available models for Nusselt number for particles with Stefan flow in a convective environment are empirical. One of the very few theoretical models (of Eq. 11) (Murphy and Shaddix, 2003) developed for the Nusselt number of particles with Stefan flow is for a *quiescent* environment and is based on a constant property assumption. Therefore, there are no models for Stefan flow in a convective environment based on physical interpretation while considering variation of properties.

2.3. Drag coefficients at high temperature differences.

The drag coefficient is defined as $C_D = F/(0.5\rho U^2 A)$, where F is the drag force, A is the cross-sectional area of the particle, ρ is the density of the fluid and U is the velocity difference between the particle and the fluid. There are many correlations available to calculate fluid drag on a solid spherical object. However, most of these models have been developed for isothermal or close to isothermal conditions. This makes these models fail at high temperature differences, since variations of properties have to be considered in order to accurately calculate the drag. The Schiller-Naumann model Schiller and Naumann (1935) for the drag coefficient, given as:

$$C_D = \frac{24}{\mathrm{Re}}(1 + 0.15\mathrm{Re}^{0.687}), \tag{14}$$

is a widely used drag model. Recently, Ellendt et al. Ellendt et al. (2018) have suggested a correction factor (ϕ) for the Schiller-Naumann correlation considering non-isothermal effects:

$$\begin{aligned} C_D &= \frac{24}{\mathrm{Re}}(1 + 0.15\mathrm{Re}^{0.687})\phi; \\ \phi &= 0.273(1 - 0.883^{\mathrm{Re}})\left(\frac{\rho_\infty}{\rho_p} - 1\right) + 1, \end{aligned} \tag{15}$$

when $1 < \mathrm{Re} < 130$. Here, the Reynolds number is evaluated at the surface temperature of the sphere, ρ_∞ is the density of the fluid in the far-field and ρ_p is the density of the fluid at the particle surface. The fluid density entering the expression for the drag coefficient ($C_D = F/(0.5\rho U^2 A)$) is at far-field conditions.

2.4. Effects of Stefan flow on drag coefficients.

Similar to the Nusselt number, the models developed for the combustion and evaporation of sprays are available for the drag coefficient under the influence of a Stefan flow (Yuen and Chen, 1976; Eisenkalam et al., 1967; Renksizbulut and Yuen, 1983b). One common approach is the so-called one-third rule proposed by Yuen and Chen Yuen and Chen (1976). The one-third rule uses ordinary drag models, for example the one of Schiller-Naumann Schiller and Naumann (1935) (see Eq. (14)), for an evaporating droplet, but with the Reynolds number calculated as:

$$\mathrm{Re} = \frac{\rho_\infty U D}{\mu_t}, \tag{16}$$

where μ_t is the dynamic viscosity obtained at the reference temperature, as given by Eq. (3), with a weight factor of $t = 1/3$. This model is applicable in the range of $1 < \mathrm{Re} < 2000$ and $0 < B_T < 3$. The same result was confirmed by Renksizbulut and Yuen Renksizbulut and Yuen (1983b) for an evaporating droplet from their simulations. However, the approach described above does not include a dependency on the Stefan velocity and is therefore not expected to be suitable unless the Stefan flow velocity is small compared to the velocity of the mean flow.

Studies of the effect of Stefan flow on the drag coefficient for generalized cases have always assumed isothermal conditions as per the authors knowledge. Most recent works are done by Jayawickrama et al. Jayawickrama et al. (2019), Kestel Kestel (2016) and Miller & Bellan Miller and Bellan (1999). The latter two have developed empirical models for the drag coefficient of a spherical object

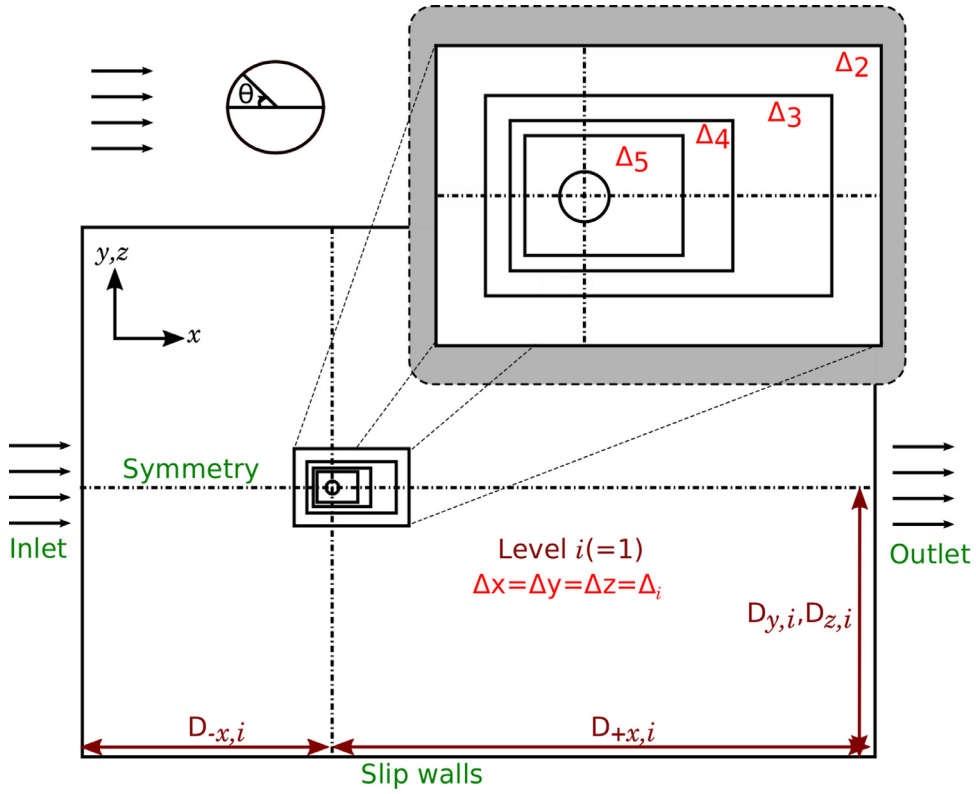

Fig. 1. Computational domain for the simulations. Δ_i, $i = 1$ to 5 representing the coarsest mesh to finest mesh. $D_{-x,i}$ is the distance from the centre of the sphere to negative x-direction and $D_{+x,i}$ is the distance from the centre of the sphere to positive x-direction in level i (See the Table 2).

with a Stefan flow. Kestel's model is applicable for a wider range of Stefan flows ($0 < \mathrm{Re_{sf}} \leqslant 20$ and $\mathrm{Re} \leqslant 200$). Both models have several fitting parameters. Jayawickrama et al. (2019) developed a model based on a physical interpretation of the drag that required only one fitting parameter. This model was validated against numerical simulations in the range of $-1 \leqslant \mathrm{Re_{sf}} \leqslant 3$ (a negative $\mathrm{Re_{sf}}$ means inward Stefan flow) and $\mathrm{Re} < 14$. All three models are applicable for isothermal conditions only. Therefore, it is important to study the effect of a Stefan flow on the drag coefficient including thermal effects as well.

3. Methodology

In the current work, numerical simulations are carried out for a flow around a static, spherical particle with constant size using OpenFOAM. The simulation domain and boundaries are shown in Fig. 1. The incoming gas flow to the simulation domain is uniform and its temperature is kept at 1400 K. A uniform Stefan flow is given as a boundary condition at the particle surface. Different cases are simulated by varying sphere surface temperature, diameter and incoming flow velocity, resulting in a variety of Reynolds numbers. Variation of properties with temperature is considered (See Appendix A for more details.). The Reynolds number is within the limit of steady, axi-symmetric flow ($\mathrm{Re} < 210$) (Johnson and Patel, 2017) and the Mach number of the flow is well below 0.1. Therefore, the flow is essentially in-compressible. The intra-particle heat transfer is not considered and the particle temperature is kept uniform both in space and time. Radiative heat transfer is also neglected. The fluid is governed by the steady, incompressible, laminar flow equations, where mass conservation yields the continuity equation as:

$$\nabla \cdot (\rho \vec{u}) = 0, \tag{17}$$

while momentum conservation gives:

$$(\rho \vec{u} \cdot \nabla)\vec{u} = -\nabla p + \nabla \cdot \mu[\nabla \vec{u} + \nabla \vec{u}^{T} - \frac{2}{3}(\nabla \cdot \vec{u})\vec{I}]. \tag{18}$$

Finally, from energy conservation we get:

$$\nabla \cdot (\rho c_p \vec{u} T) = -\nabla \cdot \lambda \nabla T. \tag{19}$$

Eqs. 17, 18 and 19 were discretized using second-order schemes with the finite volume method.

3.1. Boundary conditions.

The temperature of the inlet boundary is kept at 1400 K. The exit of the domain is considered as an outflow boundary, where the gradients of the velocity and temperature are set to zero. The boundaries at the side of the domain are treated as slip walls. In the slip wall boundary condition, the velocity component normal to the wall is zero. In addition, the gradients of temperature and the other velocity components in the normal direction to the wall are also set to be zero. Along the axis of symmetry, a symmetric boundary condition is applied. In the Symmetric boundary condition, the velocity component normal to the symmetry plane and the gradients of all the other properties normal to the plane are set to zero. Only a quarter of the domain is simulated as the flow is axisymmetric.

A Cartesian mesh is used for the simulation. The immersed boundary method (IBM) was applied for the implementation of the solid boundary. In this work, the discrete forcing approach (Mittal and Iaccarino, 2005), which directly applies the presence of a solid body through boundary conditions (Jasak et al., 2014), is used. The value of any parameter of a cell that crosses the immersed boundary is calculated by interpolating values between the immersed boundary and neighboring cells (Fadlun et al., 2000). The Stefan velocity is considered as a uniform velocity normal

Table 1
Conditions maintained for far-field velocity, particle diameter and particle temperature. Far-field temperature was kept at $T_\infty = 1400$K.

Condition	Inlet velocity (m/s)	Diameter (mm)	T_p(K)	Re_f
1	0.5	1.0	400	4.88
			1200	2.66
			1600	2.10
2	3.0	0.5	400	14.64
			1200	7.98
			1600	6.31
3	3.0	1.0	400	29.29
			1200	15.98
			1600	13.74

to the immersed boundary (Dirichlet boundary condition). For an outwardly directed Stefan flow, the temperature of the outflow is equal to the surface temperature of the particle.

The pressure gradient is set to zero at the solid boundary (Neumann boundary conditions). Treatment of Neumann and Dirichlet boundary conditions in the immersed boundary method is explained in Jayawickrama et al. (2019).

3.2. Simulation conditions and procedure

For all the simulations in this work, the fluid (including the fluid of the Stefan flow) was assumed to be pure nitrogen. The inlet velocity, diameter of the particle and temperature range of the fluid and the sphere were selected based on pulverized combustion and gasification applications at atmospheric pressure. The velocity at the inlet varied between 0.5-3 m s^{-1} and the diameter of the particle is between 0.5-1.0 mm. The range of Stefan flow velocities was selected based on results from Kreitzberg et al. (2016) and Umeki et al. (2012) for devolatilization and char conversion of biomass. The choice of bulk fluid temperature (1400 K) is based on the range of typical bulk fluid temperatures observed in pilot scale experiments of entrained-flow gasification (Sepman et al., 2017). Fuel particles in entrained flow gasifiers are usually colder than the surrounding gas because of predominantly endothermic reactions and the lack of an oxygen rich atmosphere, except for the near burner zone. The particle temperature can, however, exceed the gas temperature by ca. 200 K in pulverized combustion, where oxygen is available for char combustion reactions (Li et al., 2018). Therefore, we selected three different fuel particle temperatures (T_p =400, 1200, and 1600 K), each representing drying, char gasification, and char oxidation stages, respectively. The particle temperatures and far-field conditions studied in this work are shown in Table 1.

We used the OpenFOAM environment *foam-extend*-4.0 (Weller et al., 1998) for the simulations. The immersed boundary solver for incompressible, steady-state conditions was modified to account for non-isothermal, variable density and variable property conditions. The solver uses quadratic interpolation (Jasak et al., 2014) for the reconstruction of the solid phase boundary conditions into the closest fluid cells.

The preliminary domain size and mesh resolution was selected based on previous studies (Jayawickrama et al., 2019; Constant et al., 2017; Richter and Nikrityuk, 2012) for isothermal flow around a sphere. The inlet conditions and Stefan flow velocities are similar to the ones used for the isothermal simulations in our previous work (Jayawickrama et al., 2019). Therefore, the domain size is unchanged for the current non-isothermal simulations ($64D \times 32D \times 32D$). There are, however, two main differences in the non-isothermal cases compared to the isothermal cases.

The first difference is that a reduction (increase) of particle temperature increases (decreases) the Reynolds number (Re), resulting in a thinner (thicker) boundary layer for non-isothermal conditions. Mesh refinement tests therefore had to be carried out. The tests were carried out with the highest Reynolds number conditions (condition 3 of Table 1 with particle temperature 400K) and with the smallest possible boundary layer thickness (inward Stefan flow condition). Two mesh refinement levels were tested, as shown in Table 2 (Mesh I and Mesh III).

Table 2
Distance from the centre of the particle in diameters (D) in the computational domain (See Fig. 1).

(a) Mesh I				
i	$D_{-x,i}$	$D_{+x,i}$	$D_{y,i}, D_{z,i}$	Δ_i/D
1	16	48	16	0.32
2	3	6	3	0.16
3	2	5	2	0.08
4	1.5	3	1.5	0.04
5	1.2	2	1.2	0.02
(b) Mesh II				
i	$D_{-x,i}$	$D_{+x,i}$	$D_{y,i}, D_{z,i}$	$Delta_i/D$
1	16	48	16	0.32
2	6.5	12	6.5	0.16
3	5.5	10	5.5	0.08
4	4.5	6	4.5	0.04
5	3.5	4	3.5	0.02
(c) Mesh III				
i	$D_{-x,i}$	$D_{+x,i}$	$D_{y,i}, D_{z,i}$	Δ_i/D
1	16	48	16	0.16
2	3	6	3	0.08
3	2	5	2	0.04
4	1.5	3	1.5	0.02
5	1.2	2	1.2	0.01

The other difference between the isothermal and non-isothermal cases is due to the difference between the thermal (δ_{th}) and the viscous boundary layer thickness (δ_{vis}). As the Prandtl number (Pr) is less than 1, the thermal boundary layer thickness is larger than the viscous boundary layer thickness ($\delta_{th} > \delta_{vis}$). Therefore, the size of the mesh refinement regions have to be examined. This was carried out for the lowest Reynolds number condition (condition 1 of Table 1 with particle temperature 1600K) with the largest possible boundary layer thickness (highest outward Stefan flow). Two refinement region sizes were tested, which is shown in Table 2 (Mesh I and Mesh II). Difference between Mesh I, II and III were very small in C_D and Nu and the velocity and temperature fields around the boundary layer were also identical when comparing all the meshes. Therefore, Mesh III was used for the simulations.

Table 3 shows the selection of mesh refinement levels and size of refinement regions used for the simulations in this paper. The final mesh for all the conditions was Mesh III with the highest refinement $0.01D$.

3.3. Estimation of drag coefficient and Nusselt number

The drag coefficient is a dimensionless quantity used to represent forces acting on the surface of a body immersed in a fluid. For a spherical body with radius R, it can be calculated as:

$$C_{D,f} = \frac{\vec{F}_{P,x} + \vec{F}_{visc,x}}{\frac{1}{2}\rho_f U_\infty^2 (\pi R^2)}, \tag{20}$$

where ρ_f is the fluid density of film condition. The pressure and viscous forces are given as

$$\vec{F}_p = \oint_S p_p \vec{n}\, ds, \tag{21}$$

and

$$\vec{F}_{visc} = -\oint_S \mu_p (\nabla \vec{u} + \nabla \vec{u}^T)\vec{n}\, ds, \tag{22}$$

Table 3
Mesh refinement results and refinement domain size results as explained in section 3.2. The drag (C_D) and Nusselt number (Nu) calculated at far-field conditions and Stefan Reynolds number (Re_{sf}) calculated at particle surface condition.

Re_{sf}	Mesh	C_D	Error (% of mesh III or II)	Nu_∞	Error (% of mesh III or II)
-7.98	mesh I	3.01	10.12	5.40	0.15
	mesh III	3.36	-	5.39	-
2.36	mesh I	10.52	0.25	2.16	2.44
	mesh II	10.55		2.11	-
	mesh III	10.94		2.16	-

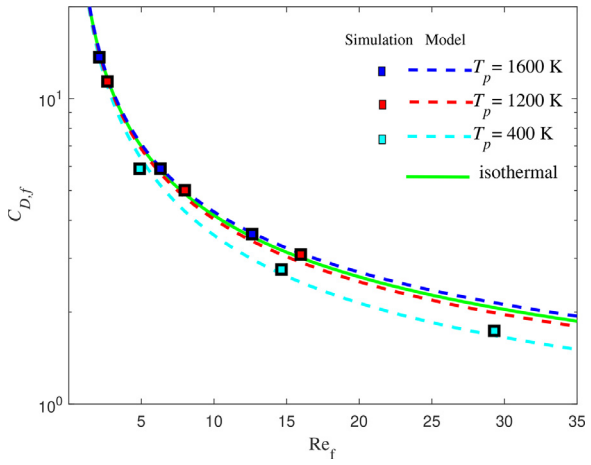

Fig. 2. Drag coefficient (C_D) at film condition for the case where there is no Stefan flow. Lines: Correlations of Ellendt et al. Ellendt et al. (2018) at different particle temperatures (400 K,1200 K,1600 K), symbols: results from our numerical simulations. Green: isothermal. Cyan: $T_p = 400$ K. Red: $T_p = 1200$ K. Blue: $T_p = 1600$ K.

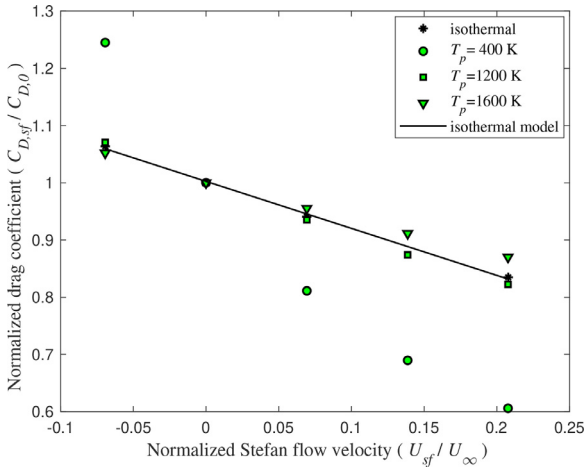

Fig. 3. Normalized drag $C_{D,sf}/C_{D,0}$ at film condition and Normalized Stefan flow velocity U_{sf}/U_∞. $C_{D,0}$ is the drag coefficient without Stefan flow. Simulation conditions: U_∞=3.0 m s^{-1}, T_∞ = 1400 K, and D=1.0 mm.

respectively. Here, the integration is over the surface S of the particle. In the above, p_p is the extrapolated pressure at the particle surface. Only the components $\vec{F}_p$ and $\vec{F}_{visc}$ in the direction of the mean flow are accounted for when calculating the drag coefficient, since the other components are canceled due to symmetry. The Nusselt number is calculated based on the overall difference in enthalpy flux at the boundaries of the simulation domain. Here, the far-field based Nusselt number is calculated as follows:

$$Nu_\infty = \frac{(\rho \vec{u}\, c_p T S)_{in} + \vec{u}_{sf}(\rho c_p T S)_{sph} - (\int(\rho \vec{u}\, c_p T)\vec{n}\, dS)_{out}}{S_{sph}(T_p - T_\infty)} \times \frac{2R}{\lambda_\infty}, \tag{23}$$

where subscripts *in, out* and *sph* refers to the conditions at the inlet boundary, the outlet boundary and the particle surface, respectively, and S is the surface area of the relevant boundary.

3.4. Validation

In order to validate the code, simulations were carried out to examine if the code reproduces known results both for the drag coefficient and the Nusselt number.

For the validation of the code with respect to the drag coefficient, non-isothermal simulations *without* Stefan flow were carried out. The drag coefficients obtained from the simulations based on Eq. 20 were compared with the model suggested by Ellendt et al. Ellendt et al. (2018) (see Eq. 15). As shown in Fig. 2, the numerical results show good agreement with the model of Ellendt et al. Please note that, when determining the model predictions, the Reynolds number is based on film conditions.

We are interested in the Nusselt number at strongly non-isothermal conditions, i.e., where the temperature difference between the particle surface and the far-field is high ($>$ 100 K). In order to validate the code with respect to the Nusselt number, simulations were carried out with a strong temperature difference, but without Stefan flow. The results were compared with the Ranz-Marshall model (Eq. 2), which is applicable for strongly non-isothermal conditions (see section 2.1). Table 4 shows a good agreement between the numerical results and the model data.

4. Results and Discussion

4.1. The effect of Stefan flow on the drag coefficient under non-isothermal conditions

By comparing the simulation results obtained at isothermal and non-isothermal conditions, it is possible to isolate the physical effects of the Stefan flow (*e.g.* due to the change in boundary layer thickness) from thermal effects (*e.g.* variation of thermophysical properties due to the change in temperature). Figure 3 shows the normalized drag coefficient ($C_{D,sf}/C_{D,0}$) against normalized Stefan flow velocity (U_{sf}/U_∞) for both isothermal and non-isothermal conditions (condition 3 of Table 1).

The drag coefficient is normalized by the corresponding drag as obtained *without* a Stefan flow ($C_{D,0}$). Here, $C_{D,0}$ and $C_{D,sf}$ are calculated based on film condition (See Eq. 20). As can be seen from the figure, the temperature difference has a significant effect on the slope of the curve, especially for high temperature differences. The drag reduction by the Stefan flow is more significant when the particle temperature is lower than the surrounding gas ($T_p < T_\infty$) and vice versa. The same behavior can be observed (not shown here) for conditions 1 and 2 (see Table 1) as well. It means that apart from the physical effects of the Stefan flow, the thermal effect has to be considered to describe the change of C_D for non-isothermal conditions.

Table 4
Comparison of Nusselt numbers (Nu) and the drag coefficient (C_D) without Stefan flow from simulations and the Ranz-Marshall model (Eq. 2)), respectively the model of Ellendt et al. (Eq. 15). Far-field temperature (T_∞) is 1400 K for all the cases. Conditions 1-3 are listed in Table 1, while conditions 4-5 are presented in the following: condition 4: $D = 1.0$ mm and $U_\infty = 5.94$ m s^{-1}, Condition 5: $D = 1.0$ mm and $U_\infty = 11.88$ m s^{-1}

Condition	T_p K	$\mathrm{Re_f}$ -	Nu *Sim*	*Model*	Error %	$C_{D,f}$ *Sim*	*Model*	Error %
1	400	4.88	3.16	3.32	4.8	5.90	6.48	8.95
	1200	2.66	2.84	2.89	1.7	11.39	11.53	1.22
	1600	2.10	2.74	2.78	1.4	13.67	14.38	4.98
2	400	14.65	4.04	4.28	5.6	2.76	2.67	1.34
	1200	7.99	3.57	3.55	0.6	5.01	4.76	2.15
	1600	6.31	3.41	3.35	1.8	5.90	5.95	0.30
3	400	29.29	5.16	5.23	1.3	1.74	1.68	0.92
	1200	15.98	4.34	4.20	3.3	3.09	2.92	1.55
	1600	12.63	4.06	3.91	3.8	3.60	3.64	0.24
4	1600	25.0	4.95	4.69	5.5			
5	1600	50.0	6.22	5.80	7.2			

The thermal effects of the Stefan flow can be studied by investigating Fig. 4, which shows the variation of the velocity and temperature fields in the boundary layer. Without the Stefan flow (blue lines), the velocity gradient of the non-isothermal case ($T_p < T_\infty$) is slightly larger than that of the isothermal case. Nevertheless, we can see from Fig. 2 that the drag coefficient for $T_p < T_\infty$ (non-isothermal case) is lower than for the isothermal case. This is because the contribution from the change in thermophysical parameters is more significant than the change in boundary layer thickness (Eq. 20). To be more specific: one would expect the drag coefficient to increase when the boundary layer gets thinner (higher velocity gradients), but this effect is more than compensated by the decrease in viscosity due to the lower temperature. In essence, the local Reynolds number is increased when the particle temperature becomes lower than the far-field temperature, and it is clear from Fig. 2 that the drag coefficient decrease with increasing Re_f.

In contrast, the same non-isothermal case shows a more pronounced expansion of the velocity boundary layer with an outward Stefan flow (red lines) than does the isothermal case. This pronounced change in the velocity is due to the expansion of the gas from the Stefan flow as it is heated. Since it is the *velocity* of the Stefan flow that is kept constant between different cases, the total mass flux due to the Stefan flow is much higher for the non-isothermal case (since the fluid density is more than three times higher at 400 K than at 1400 K). This means that as the initially cold gas emitted from the particle at 400 K is heated up, it accelerates and pushes the boundary layer outwards. In fact, the normalized temperature plot in Fig. 4b shows the decrease in gas temperature near the particle surface with outward Stefan flow. As for the inward Stefan flow, both velocity and thermal boundary layers showed exactly opposite trends from the outward Stefan flow, i.e. steeper velocity gradient and thinner thermal boundary layer. These observations imply the importance to consider the change in thermophysical parameters when modelling the drag coefficient under non-isothermal conditions. Therefore, the model developed in our previous paper (Jayawickrama et al., 2019), which was based on isothermal simulations, needs to be extended to consider the effect of the variation of thermo-physical properties.

Our previous study under isothermal conditions (Jayawickrama et al., 2019) showed that the drag coefficient changes due to a Stefan flow. This change is primarily caused by a modification of the viscous forces due to the change in boundary layer thickness. Following the idea in Jayawickrama et al. (2019), the current study uses a simple model for the effect of a Stefan flow on the drag coefficient. It is related to the change in the volume of the boundary layer due to the Stefan flow, and is

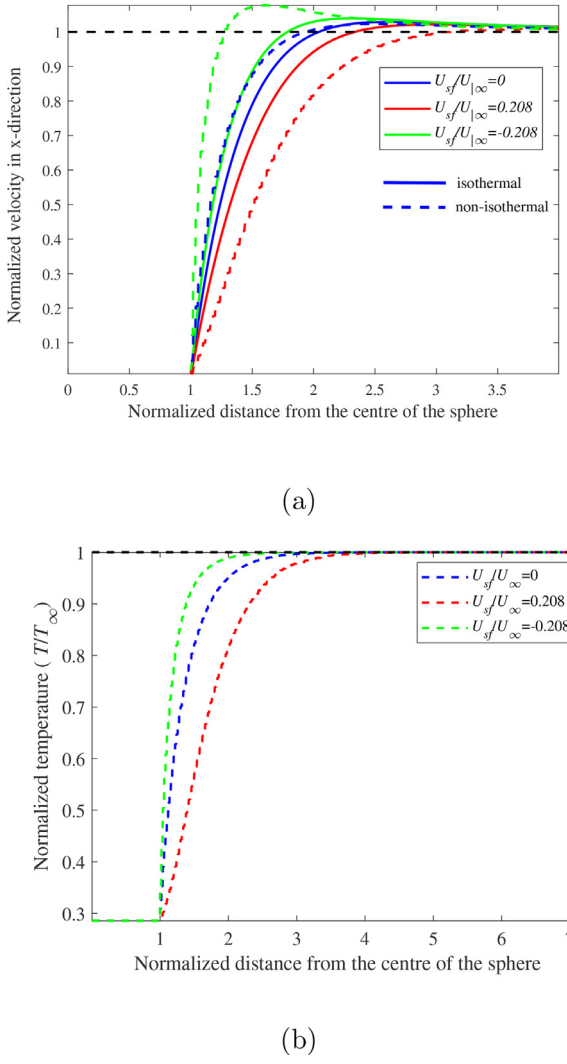

Fig. 4. (a) Normalized velocity in the mean flow direction (U_x/U_∞); (b) Normalized temperature (T/T_∞). Both figures are drawn as functions of the normalized distance from the centre of the sphere (y/R) along the y-axis ($\theta = 90^\circ$). Simulation conditions: U_∞=3.0 m s^{-1}, T_∞ = 1400 K, and D=1.0 mm. Solid lines: isothermal and Dashed lines: non-isothermal results (T_p = 400 K).

proposed as:

$$C_{D,sf} = C_{D,0} \times C_{D,r}, \tag{24}$$

when $C_{D,0}$ is the drag coefficient under non-isothermal conditions without a Stefan flow (see e.g. Eq. (15)), and $C_{D,r}$ is a correction term that accounts for the effects of a Stefan flow, in addition to any thermal effects of this Stefan flow. This correction term takes into account two effects: one is due to the temperature difference between the particle surface and the far-field while the other is due to the variation of the temperature field due to the Stefan flow. Both effects can be accounted for by using a modified temperature ($\tilde{T}$) based on the volumetric contribution of the Stefan flow (V_{sf}) and its temperature ($T_{sf} = T_p$), and the volume of the boundary layer without Stefan flow (V_B) and its temperature ($T_f = \frac{T_\infty + T_p}{2}$);

$$\tilde{T} = \frac{V_B T_f + V_{sf} T_p}{V_B + V_{sf}}, \tag{25}$$

where

$$V_{sf} = 4\pi R^2 U_{sf} \tau \tag{26}$$

is the added volume due to the Stefan flow,with the flow time-scale given as:

$$\tau = \frac{2(R+\delta)}{U_\infty}. \tag{27}$$

Furthermore, the volume of the boundary layer is given as:

$$V_B = \frac{4}{3}\pi (R+\delta)^3 - \frac{4}{3}\pi R^3, \tag{28}$$

when

$$\delta = \frac{2AR}{\sqrt{\mathrm{Re}_f}}, \tag{29}$$

is the classical boundary layer thickness, where

$$\mathrm{Re}_f = \frac{\rho_f U_\infty d}{\mu_f} \tag{30}$$

and A is a model constant. By substituting V_{sf} and V_B in Eq. 25 with the corresponding expressions found in Eq. 26 and 28 we obtain:

$$\tilde{T} = \frac{T_f + \frac{U_{sf}}{U_\infty} f(\mathrm{Re}_f) T_{sf}}{1 + \frac{U_{sf}}{U_\infty} f(\mathrm{Re}_f)}, \tag{31}$$

where

$$f(\mathrm{Re}_f) = 3\left(1 + \frac{2A}{\sqrt{\mathrm{Re}_f}}\right) \frac{1}{\left(\frac{3A}{\sqrt{\mathrm{Re}_f}} + 6\left(\frac{A}{\sqrt{\mathrm{Re}_f}}\right)^2 + 4\left(\frac{A}{\sqrt{\mathrm{Re}_f}}\right)^3\right)}. \tag{32}$$

Now, $\tilde{T}$ will be used to calculate the drag coefficient without Stefan flow ($\tilde{C}_{D,0}$) such that the non-isothermal model for $C_{D,sf}$ becomes:

$$C_{D,sf} = \tilde{C}_{D,0} \times C_{D,r}, \tag{33}$$

where $\tilde{C}_D$ is calculated from the modified Schiller-Naumann equation (Eq. 15) for non-isothermal conditions:

$$\tilde{C}_{D,0} = \frac{24}{\tilde{\mathrm{Re}}}\left(1 + 0.15\tilde{\mathrm{Re}}^{0.687}\right)\phi; \qquad \phi = 0.273\left(1 - 0.883^{\tilde{\mathrm{Re}}}\right)\left(\frac{\rho_\infty}{\rho_p} - 1\right) + 1, \tag{34}$$

where $\tilde{\mathrm{Re}}$ is the Reynolds number calculated with properties at $\tilde{T}$. $C_{D,r}$ is calculated based on the model developed from isothermal simulations (Jayawickrama et al., 2019) where:

$$C_{D,r} = \frac{V_B}{V_{sf} + V_B} = \frac{1}{1 + \frac{U_{sf}}{U_\infty} f(\mathrm{Re}_f)}. \tag{35}$$

In the above, the tilde over C_D is used to highlight that it is based on properties calculated at $\tilde{T}$. The constant A is calculated using non-linear least-squares regression to minimize the error between the model and the simulation results (*nlinfit* in MATLAB). The final value of A is 2.93.

Fig. 5, which shows the drag coefficient as a function of the Stefan flow Reynolds number, compares the above model with simulation results. The model is an extension of the previous isothermal model presented in Jayawickrama et al. (2019). This new model captures the effects of non-isothermal, uniform bulk flow and uniform Stefan flow. Model data and simulation results are matching well and it has only one fitting parameter (A). The model has a good qualitative performance for both negative and positive Stefan flow conditions, and it is based on a physical interpretation of thermal effects due to property variations and the Stefan flow, and physical effects due to pressure, viscosity and Stefan flow.

The (relative) root-mean-square error (Eq. 36) with all the data in Fig. 5 was 9.6%. The error was relatively high for $T_p = 400$ K (Fig. 5a), with the maximum value reaching 28%. When only considering the data from the temperature difference of 200 K (Fig. 5b-c), the maximum relative error of the model was 6% and the root-mean-square error was 4.6%. Root-mean-square error ($RMSE_{C_d}$) is calculated as follows:

$$RMSE_{C_d} = 100 \times \sqrt{\frac{\left[\Sigma\left(\frac{C_{d,model} - C_{d,simulations}}{C_{d,simulations}}\right)^2\right]}{n}}, \tag{36}$$

where $C_{d,model}$ is the value predicted by the model Eq. 33-(35) and $C_{d,simulations}$ is the value calculated from the simulations and n is the number of simulations considered.

The models are tested and validated for the particle Reynolds number range of $2 \leqslant \mathrm{Re}_f \leqslant 30$, Stefan Reynolds number range of $-8 \leqslant \mathrm{Re}_{sf,p} \leqslant 25$, and temperature range of $400K \leqslant T_p \leqslant 1600K$ with uniform Stefan flow. The developed model should be applicable for the valid temperature ranges of the modified Schiller-Naumann model (Eq. 34). However, one should be careful when extrapolating the applicability beyond the range of validation conditions. For example, the model might not be valid at higher particle Reynolds number due to flow separation or the change in the relative magnitude between the pressure force and the viscous force.

4.2. Nusselt number with Stefan flow

Murphy & Shaddix Murphy and Shaddix (2003) has developed a theoretical model that accounts for the effect of a Stefan flow when calculating the Nusselt number of a sphere immersed in a quiescent fluid (See Eq. 11). In their model, the Nusselt number is calculated as $\mathrm{Nu}_M = \mathrm{Nu}_0 f_{\mathrm{corr}}$, where $\mathrm{Nu}_0 = 2$ is the Nusselt number of a spherical particle with no Stefan flow in a quiescent fluid and f_{corr} is a correction term that accounts for the effect of the Stefan flow. One way to apply this model directly for the cases with convective flows is to replace the Nusselt number, Nu_0, with the one with a convective flow, as given by e.g. the Ranz-Marshall model. However, the prediction with this approach does not describe the simulation results. The same observation was discussed by Kestel Kestel (2016), who proceeded to develop an empirical model with several fitting parameters Eqs. 12-(13).

As discussed in the previous section, the temperature in the boundary layer changes due to the Stefan flow, especially when the temperature differences are significant. This change should be reflected in the characteristic temperature when calculating the Nusselt number. In this work, we apply a multiplication law to describe the effect of a Stefan flow (by Eq. 11) and the effect of a convective flow (Eq. 2), but considering the change in characteristic temperature. This approach in practice calculates the Nusselt

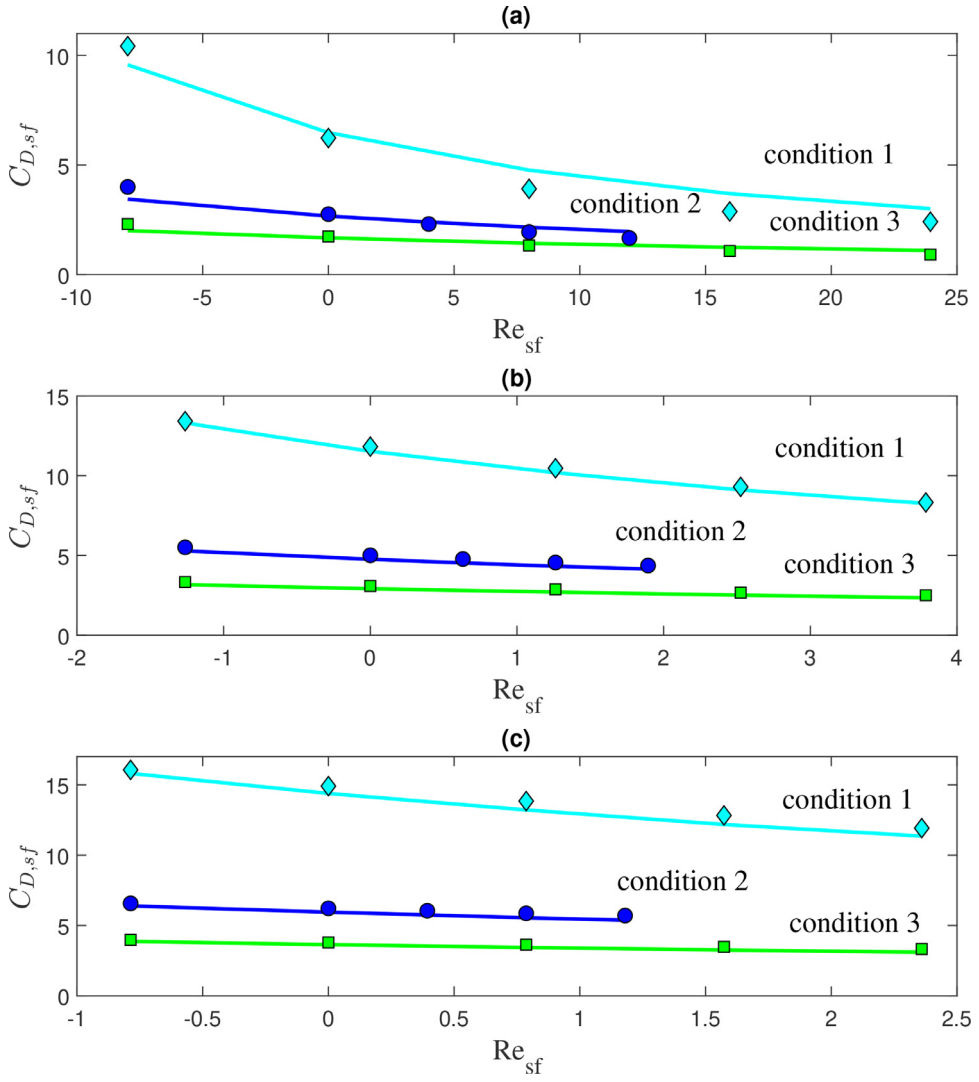

Fig. 5. Comparison of the drag coefficient from the model, i.e. Eqs. 31-35, (lines) and the simulations based on $\tilde{T}$ (symbols). Particle temperature (T_p) is (a) 400 K (b) 1200 K or (c) 1600 K. Condition 1: U_∞=0.5 m s^{-1}and D=1.0 mm. Condition 2: U_∞=3.0 m s^{-1}and D=0.5 mm. Condition 3: U_∞=3.0 m s^{-1}and D=1.0 mm.

number based on the thermophysical properties using the volume averaged temperature derived earlier (Eq. 31). The model for the Nusselt number needs to be applicable for convective flows around a sphere with high temperature differences. Here, we have used a Ranz-Marshall type model by parameter fitting the original Ranz-Marshall model with simulation data without Stefan flow, to obtain:

$$\tilde{\mathrm{Nu}} = 2 + 0.570\tilde{\mathrm{Re}}^{0.537}\tilde{\mathrm{Pr}}^{1/3}, \tag{37}$$

where Re and Pr were calculated based on the volume averaged temperature, $\tilde{T}$, as given in Eq. 31. Now we can replace the Nusselt number without Stefan flow (Nu) in Murphy & Shaddix model (Eq. 11) with the model presented in Eq. 37, such that the final model for Nu, accounting for non-isothermal effects and Stefan flow reads as:

$$\mathrm{Nu}_{sf,f} = \tilde{\mathrm{Nu}}\frac{q}{e^q - 1}, \tag{38}$$

where $q = \frac{\mathrm{Pr}_f \mathrm{Re}_{sf,p}}{\tilde{\mathrm{Nu}}}$ and $\mathrm{Nu}_{sf,f}$ calculated based on film condition for the thermal conductivity (λ_f). The Stefan flow Reynolds number (Re_{sf}) is calculated based on particle surface condition while the Prandtl number (Pr) is calculated based on film condition.

It is clear that the volume averaged temperature must lie between the particle temperature (T_p) and the far-field temperature (T_∞). From the definition of the volume averaged temperature, as given by Eq. 25 (respectively Eq. 31), it can be shown that this is not the case when $V_{sf}/V_B < -0.5$. (This corresponds to a situation where there is a very strong *inward* Stefan flow.) This means that the expression given by Eq. 25 can not be used to define the volume averaged temperature for such a condition. Therefore, the volume averaged temperature is assumed to be equal to the far-field temperature when $V_{sf}/V_B < -0.5$. This means that,

$$\tilde{T} = \begin{cases} \frac{T_f + \frac{U_{sf}}{U_\infty} f(\mathrm{Re}_f) T_{sf}}{1 + \frac{U_{sf}}{U_\infty} f(\mathrm{Re}_f)} \quad \text{(Eq.31)} & \text{for } V_{sf}/V_B \geqslant -0.5, \quad (39) \\ T_\infty & \text{for } V_{sf}/V_B < -0.5, \quad (40) \end{cases}$$

where $f(Re_f)$ is calculated from Eq. 32 and $A = 0.4$.

To validate the model, the Nusselt number was calculated from the simulation with the conditions 1, 2, and 3 (see Table 1) including one negative Stefan flow case with $V_{sf}/V_B < -0.5$. Fig. 6 depicts the comparison between simulation results (symbols) and the predictions obtained with the model presented in Eq. (38) (lines).

The (relative) root-mean-square error (Eq. 36 after replacing the term C_d with Nu) with all the data in Fig. 6 was 12.6%. The error was relatively high for $T_p = 400$ K (Fig. 6a), with the maximum value reaching 73%. When only considering the data from the tem-

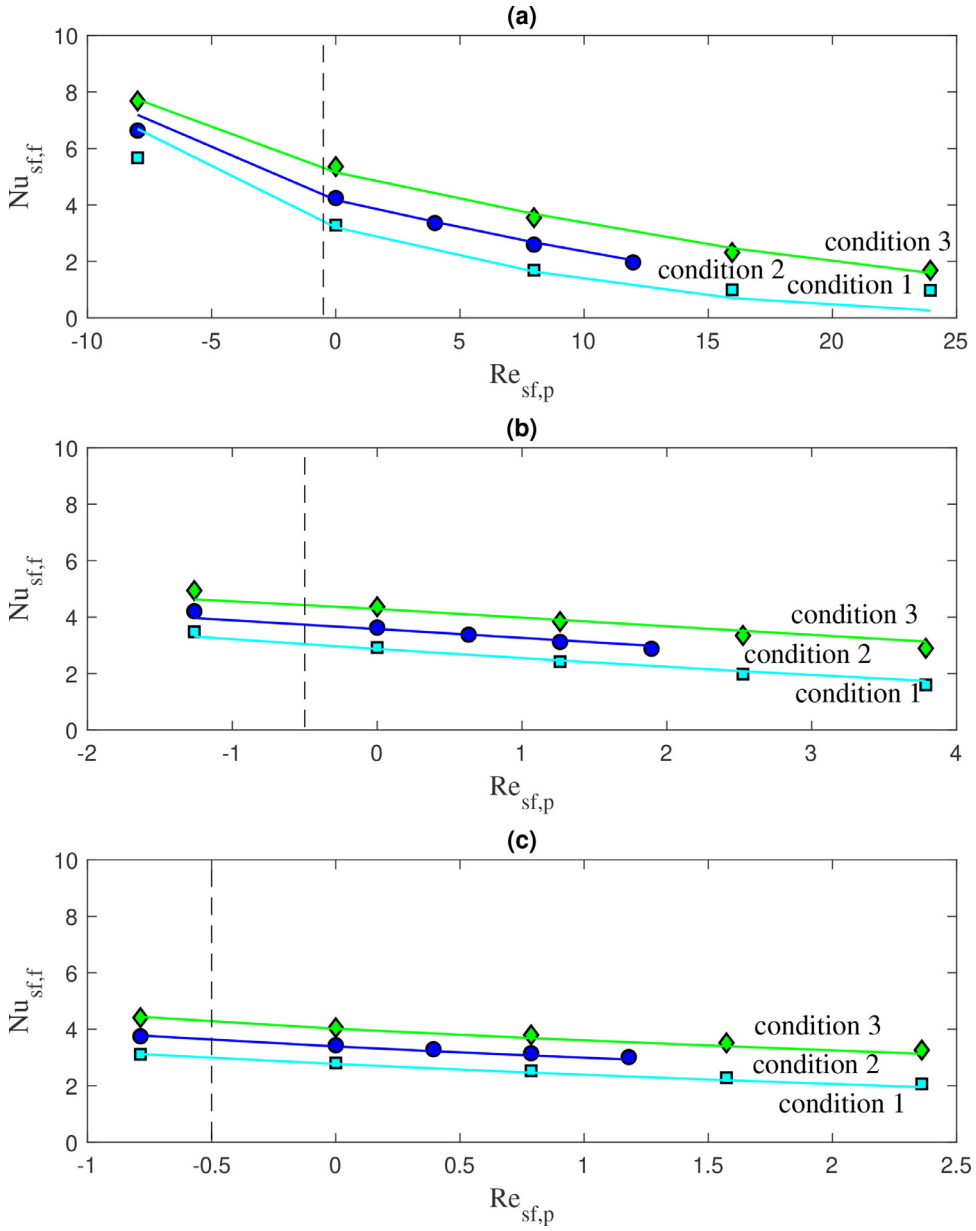

Fig. 6. The Nusselt number comparison between the model (Eq. 38-lines) and simulation (symbols) data with Stefan flow. Particle temperature (T_p) is (a) 400 K (b) 1200 K or (c) 1600 K. Condition 1: U_∞=0.5 m s^{-1}and D=1.0 mm. Condition 2: U_∞=3.0 m s^{-1}and D=0.5 mm. Condition 3: U_∞=3.0 m s^{-1}and D=1.0 mm.

perature difference of 200 K (Fig. 6b-c), the maximum relative error of the model was 9% and the root-mean-square error was 3.8%.

The model is developed for calculating the Nusselt number for a spherical particle with uniform Stefan flow, immersed in a uniform convective flow. It was validated for the Reynolds number (Re_f) $2 \leqslant \mathrm{Re}_f \leqslant 30$, Stefan Reynolds number ($\mathrm{Re}_{sf,p}$) $-8 \leqslant \mathrm{Re}_{sf,p} \leqslant 25$ and temperature range 400 K-1600 K for nitrogen gas atmosphere. The parameters for the Nusselt number without Stefan flow (Eq. 37) were estimated by fitting the simulation data presented in this study. Different sets of parameters might be applicable for different Reynolds number and temperature ranges.

The model for the drag coefficient and the Nusselt number were both developed by assuming that the change in temperature inside the boundary-layer occurs due to variations in Stefan flow velocity, Stefan flow temperature and far-field temperature alone. This would not be the case when there are other phenomena that affect the boundary-layer temperature, such as e.g., homogeneous reactions. The model is based on the assumption that the pressure force and the viscous force are of the same order of magnitude and that only the viscous force is affected by the Stefan flow (see Jayawickrama et al. (2019)). This might not be true for higher Reynolds numbers.

5. Conclusions

The effect of a Stefan flow on the drag coefficient and Nusselt number was studied for a uniform flow around a spherical particle. The effect was investigated at non-isothermal conditions using resolved numerical simulations. Particle diameter, slip velocity, particle temperature, and Stefan flow velocity from/to the particle have been varied during the simulations. The range of Stefan Reynolds number of $-8 \leqslant \mathrm{Re}_{sf,p} \leqslant 25$, Reynolds number of $2 \leqslant \mathrm{Re}_f \leqslant 30$ and particle temperatures (T_p) of 400 K, 1200 K and 1600 K were considered in the simulations. The far-field temperature (T_∞) was kept constant at 1400 K.

The sensitivity of the drag coefficients on the Stefan flow was significantly different between isothermal and non-isothermal conditions. The effect of variation in thermophysical properties, especially at high temperature differences (between particle and far-field), is emphasized. This difference makes isothermal models less accurate for estimation of the drag coefficient.

Our previous model, developed for the drag coefficient with Stefan flow at isothermal conditions, therefore was modified for non-isothermal conditions. The refined model (presented in Eq. 33) introduced the volume averaged film temperature ($\tilde{T}$) to describe the change of thermophysical parameters in the boundary layer by a Stefan flow under non-isothermal conditions. The model is based on the physical interpretations and shows a good agreement with the simulation data. It kept the number of fitting parameter to one, which represents the relationship between the boundary layer thickness and the particle Reynolds number.

Similarly, a new model (see Eq. (38)) that describes the effect of a Stefan flow on the Nusselt number was developed by using the volume averaged temperature ($\tilde{T}$) in combination with models that describe convective flow effects and Stefan flow effects on the Nusselt number. The model agrees well with the simulation data with a single fitting parameter, which represents the relationship between boundary layer thickness and particle Reynolds number.

Declaration of Competing Interest

The authors declare that they have no known competing financial interests or personal relationships that could have appeared to influence the work reported in this paper.

CRediT authorship contribution statement

Thamali R. Jayawickrama: Conceptualization, Methodology, Software, Validation, Formal analysis, Writing - original draft, Visualization. **Nils Erland L. Haugen:** Conceptualization, Writing - review & editing, Supervision, Funding acquisition. **Matthaus U. Babler:** Writing - review & editing, Supervision, Funding acquisition. **M.A. Chishty:** Writing - review & editing, Supervision. **Kentaro Umeki:** Conceptualization, Methodology, Resources, Writing - review & editing, Supervision, Project administration, Funding acquisition.

Acknowledgment

The authors are grateful to the Swedish Research Council (Vetenskapsrådet) for financial support for the study (grant number: 2016-07213). The simulations were performed on resources, *Kebnekaise*, provided by the Swedish National Infrastructure for Computing (SNIC) at High Performance Computing Center North (HPC2N). The authors thank all the staff of HPC2N for the technical assistance and specially to Pedro Ojeda May for the support with OpenFOAM. Furthermore, M.U.B. thanks the Swedish for Gasification Center and its industrial and academic partners for financial suppport. N.E.L.H. acknowledge the Research project Gaspro, financed by the research council of Norway (267916) the European Union's Horizon 2020 research and innovation programme(No 764697). This work also benefitted from computer resources made available through Norwegian NOTUR program, under award NN9405K.

Appendix A. Gas properties

Variation of thermal and physical properties of nitrogen (N_2) with temperature were calculated as follows. Specific heat capacity(c_p) is calculated by NASA polynomials:

$$c_p = R_{c_p}(a_0 + a_1T + a_2T^2 + a_3T^3 + a_4T^4 + a_5/T + a_6/T^2), \quad \text{(A.1)}$$

Table A.5
Coefficients for calculation of heat capacity (c_p) of gas.

Coefficient	$T < 1000$ K	$T > 1000$ K
a_0	3.29868	2.92664
a_1	0.00140824	0.00148798
a_2	-3.96322×10^{-6}	-5.68476×10^{-7}
a_3	5.64152×10^{-9}	1.0097×10^{-10}
a_4	-2.44486×10^{-12}	-6.75335×10^{-15}
a_5	-1020	-922.798
a_6	3.95037	5.98053

where a_0, a_1, a_2, a_3, a_4, a_5, a_6 are one set of constants for $T > 1000$ K and another set of constants for $T < 1000$ K. R_{c_p} (=296.8048) is a constant (Table A.5).

Dynamic viscosity(μ) is calculated from Sutherland formula (Sutherland, 1893):

$$\mu = 1.67212 \times 10^{-6}\sqrt{T}/(1 + 170.672/T), \quad \text{(A.2)}$$

where μ is in Pa.s and T is in K. Density (ρ) is calculated from state equation with constant pressure;

$$\rho = pM/RT, \quad \text{(A.3)}$$

where M is the molecular weight (28.01 g/mol), p atmospheric pressure (101325 Pa) is and R is the gas constant. Thermal conductivity (λ) is calculated from following model:

$$\lambda = 4.8 \times 10^{-4}T^{0.717}, \quad \text{(A.4)}$$

where λ is in W/(K.m) and T is in K.

References

Abramzon, B., Sirignano, W.A., 1989. Droplet vaporization model for spray combustion calculations. International Journal Heat Mass Transfer 32 (9), 1605–1618.
Constant, E., Favier, J., Meldi, M., Meliga, P., Serre, E., et al., 2017. An immersed boundary method in OpenFOAM: Verification and validation. Computers and Fluids doi:10.1016/j.compfluid.2017.08.001.
Downingm, C.G., 1966. The evaporation of drops of pure liquids at elevated temperatures: Rates of evaporation and wet-bulb temperatures. AIChE Journal 12 (4), 760–766. doi:10.1002/aic.690120424. arXiv:1011.1669v3.
Eisenkalam, P., Arunachalam, S.A., Westen, J.A., 1967. Evaporation rates and drag resistance of burning drops. In: Eleventh Symposium (International) on Combustion, Vol. 11, pp. 715–728.
Ellendt, N., Lumanglas, A.M., Moqadam, S.I., Mädler, L., 2018. A model for the drag and heat transfer of spheres in the laminar regime at high temperature differences. International Journal of Thermal Sciences 133, 98–105. doi:10.1016/j.ijthermalsci.2018.07.009.
Fadlun, E.A., Verzicco, R., Orlandi, P., Mohd-Yusof, J., 2000. Combined Immersed-Boundary Finite-Difference Methods for Three-Dimensional Complex Flow Simulations. Journal of Computational Physics 161, 35–60. doi:10.1006/jcph.2000.6484.
Harpole, G.M., 1981. Droplet Evaporation in High Temperature Environments. Jouranl of Heat Transfer 103, 86–91.
Jasak, H., Rigler, D., Tukovic, Z., 2014. Design and implementation of Immersed Boundary method with discrete forcing approach for boundary conditions. In: proceedings of 6th European Congress on Computational Fluid Dynamics - ECFD VI, Barcelona, Spain, pp. 5319–5332.
Jayawickrama, T.R., Haugen, N.E.L., Babler, M.U., Chishty, M.A., Umeki, K., 2019. The effect of Stefan flow on the drag coefficient of spherical particles in a gas flow. International Journal of Multi-phase Flow 117, 130–137. doi:10.1016/j.ijmultiphaseflow.2019.04.022.
Johnson, T.A., Patel, V.C., 2017. Flow past a sphere up to a Reynolds number of 300. J. Fluid Mech 378, 19–70. doi:10.1017/S0022112098003206.
Kestel, M., 2016. Numerical Modeling of Moving Carbonaceous Particle Conversion in Hot Environments. TU Bergakademie Ph.D. thesis.
Kreitzberg, T., Pielsticker, S., Gvert, B.M., Kneer, R., 2016. CO2 and H2O Gasification under Chemically and Diffusion Controlled Conditions. In: 33rd Annual International Pittsburgh Coal Conference, Cape Town.
Li, T., Niu, Y., Wang, L., Shaddix, C., Løvås, T., et al., 2018. High temperature gasification of high heating-rate chars using a flat-flame reactor. Applied Energy 227, 100–107. doi:10.1016/j.apenergy.2017.08.075.
Miller, R.S., Bellan, J., 1999. Direct numerical simulation of a confined three-dimensional gas mixing layer with one evaporating hydrocarbon-droplet-laden stream. J. Fluid Mech 384, 293–338.
Mittal, R., Iaccarino, G., 2005. Immersed Boundary Methods. Annual Review of Fluid Mechanics 37 (1), 239–261. doi:10.1146/annurev.fluid.37.061903.175743.
Murphy, J.J., Shaddix, C.R., 2003. Effects of Stefan Flow on Heat Transfer from reacting Carbon particles. Sandia-Report 2003-8720J 1–24.

Naraslmhan, C., Gauvin, W.H., 1967. Heat and Mass Transfer to Spheres in High Temperature Surroundings. The Canadian journal of Chemical Engineering 45, 181–188.
Niazmand, H., Renksizbulut, M., 2003. Transient three-dimensional heat transfer from rotating spheres with surface blowing. Chemical Engineering Science 58, 3535–3554. doi:10.1016/S0009-2509(03)00191-X.
Nikrityuk, B., Meyer, P.A., 2014. Gasification Processes Modeling and Simulation, 1 Wiley-VCH.
Ranz, W.E., Marshall, W.R., 1952. Evaporation from drops. Chemical Engineering Progress 48 (3), 141–146.
Renksizbulut, M., Yuen, M.C., 1983. Experimental study of droplet evaporation in a high-temperature air stream. Journal of Heat Transfer 105, 384–388.
Renksizbulut, M., Yuen, M.C., 1983. Numerical Study of Droplet Evaporation in a High-Temperature Stream. Journal of Heat Transfer 105 (2), 389–397. doi:10.1115/1.3245591.
Richter, A., Nikrityuk, P.A., 2012. Drag forces and heat transfer coefficients for spherical, cuboidal and ellipsoidal particles in cross flow at sub-critical Reynolds numbers. International Journal of Heat and Mass Transfer 55 (4), 1343–1354. doi:10.1016/j.ijheatmasstransfer.2011.09.005.
Schiller, L., Naumann, A., 1935. A drag coefficient correlation. Zeitschrift des Vereins Deutscher Ingenieure 77, 318–320.
Sepman, A., Ögren, Y., Qu, Z., Wiinikka, H., Schmidt, F.M., et al., 2017. Real-time in situ multi-parameter TDLAS sensing in the reactor core of an entrained-flow biomass gasifier. Proceedings of the Combustion Institute 36 (3), 4541–4548. doi:10.1016/j.proci.2016.07.011.
Sutherland, W., 1893. The viscosity of gases and molecular force. Philosophical Magazine 507–531.
Umeki, K., Kirtania, K., Chen, L., Bhattacharya, S., et al., 2012. Fuel Particle Conversion of Pulverized Biomass during Pyrolysis in an Entrained Flow Reactor. Industrial & Engineering Chemistry Research 51, 13973–13979. doi:10.1021/ie301530j.
Weller, H.G., Tabor, G., Jasak, H., Fureby, C., 1998. A tensorial approach to computational continuum mechanics using object-oriented techniques. Computers in Physics 12, 620–631. doi:10.1063/1.168744.
Whitaker, S., 1972. Forced Convection Heat Transfer Correlations for Flow in Pipes, Past Flat Plates, Single Cylinders, Single Spheres, and for Flow in Packed Beds and Tube Bundles. AIChE Journal 18, 361–371.
Yu, J., Zhou, K., Ou, W., 2013. Effects of Stefan flow and CO oxidation on char particle combustion in O2/CO2 atmosphere. Fuel 106, 576–585.
Yuen, M.C., Chen, L.W., 1976. On drag of evaporating liquid droplets. Combustion Science Technology 14, 147–154.
Yuen, M.C., Chen, L.W., 1978. Heat-transfer measurements of evaporating liquid droplets. International Journal of Heat and Mass Transfer 21 (5), 537–542. doi:10.1016/0017-9310(78)90049-2.
Zhifu, Z., Guoxiang, W., Bin, C., Liejin, G., Yueshe, W., 2013. Evaluation of Evaporation Models for Single Moving Droplet with a High Evaporation Rate. Powder Technology 240, 95–102. doi:10.1016/j.powtec.2012.07.002.